Nanoscale insights into the influence of seawater (NaCl) on the behavior of calcium silicate hydrate

Ming-Feng Kai[1], Dong-Shuai Hou[2], Florence Sanchez[3], Chi-Sun Poon[4] and Jian-Guo Dai[5]*

1. Research Assistant Professor, Department of Civil and Environmental Engineering, The Hong Kong Polytechnic University, Hong Kong, Email: mingfeng.kai@polyu.edu.hk, ORCID: 0000-0002-7626-2328
2. Professor, Department of Civil Engineering, Qingdao University of Technology, Qingdao, China. Email: dshou@outlook.com, ORCID: 0000-0002-1252-2987
3. Professor, Department of Civil and Environmental Engineering, Vanderbilt University, Nashville, TN, USA. Email: florence.sanchez@vanderbilt.edu, ORCID: 0000-0002-1176-2751
4. Chair Professor, Department of Civil and Environmental Engineering, The Hong Kong Polytechnic University, Hong Kong. Email: chi-sun.poon@polyu.edu.hk, ORCID: 0000-0003-4912-3936
5. Professor (Corresponding author), Department of Civil and Environmental Engineering, The Hong Kong Polytechnic University, Hong Kong. Email: cejgdai@polyu.edu.hk, ORCID: 0000-0001-9904-7914

Abstract

Using seawater for concrete production is potentially advantageous from a sustainability perspective. However, the fundamental mechanisms underlying seawater-mixed concrete are far from being understood, especially from the nanoscale. Herein, molecular models are developed to study, for the first time, the influence of seawater (NaCl solutions) on the behavior of calcium silicate hydrate (C-S-H, the main binding phase of concrete). Thermodynamically, Na^+ showed a strong adsorption capacity on the C-S-H surface, resulting in the partial release of Ca^{2+} from the surface (termed as "Na−Ca cation exchange"). Mechanically, the presence of NaCl in the interlayer solutions enhanced the bond performance between the C-S-H layers because Na^+ ions provided a greater stress transfer capacity than H_2O molecules. Under shear loading, the C-S-H layers slid over each other with the interlayer solutions acting as lubricant. Increase in NaCl concentration enhanced the sliding resistance, which was attributed to the increased viscosity of the interlayer solutions and strengthening of the solid-solution interfaces. The above atomic-level findings facilitate a better understanding of the influence of seawater on concrete properties.

Keywords: Seawater; Calcium silicate hydrate; Cation exchange; Bond performance; Sliding behavior

1. Introduction

The shortage of freshwater, one of the most precious resources on earth, has become a global concern due to climate change, industrialization and urbanization.[1] However, a massive amount of freshwater (~16.6 × 10^9 m^3) is annually consumed for global concrete production, which contributes to ~18% of industrial freshwater consumption worldwide.[2] Considering the increasing shortfalls of freshwater, especially for regions that experience freshwater stress,[1] seawater-mixed concrete has gained increasing interest in recent years, which is advantageous from a sustainability perspective. Generally, seawater can be used to produce various types of concrete, including (i) plain concrete, (ii) reinforced concrete using coated steel bar (e.g. epoxy-coated steel), and (iii) reinforced concrete using fibre-reinforced polymer (FRP) bar as the reinforcement.[3-5]

A significant number of experimental studies have been carried out on seawater-mixed concrete.[6, 7] It is widely accepted that seawater, compared to freshwater, can accelerate the early-age hydration of cement, resulting in the increased formation of $Ca(OH)_2$ and a higher pH in the seawater-mixed cement paste.[8, 9] As the hydration consumes water, the pore solution in seawater-mixed cement concentrates, leading to higher sodium (Na^+) and chloride (Cl^-) ion concentrations compared to seawater.[10] It was also reported that the ionic strength of cement pore solution is increased by four times in seawater-mixed paste due to the increased Na^+ and Cl^- concentrations.[8] In addition, seawater can refine the pore structure, especially for large capillary pores (>100 nm), and reduce the porosity of the hydrated cement.[5, 6, 11-13] In terms of mechanical properties, it has been shown that seawater-mixed concrete exhibits 5–30% higher early strength than freshwater-mixed concrete within the first 3 days, due to the accelerated hydration at early stages.[6, 14] However, the effect of seawater on the long-term strength of concrete is still unclear and contradictory results have been reported. For example, Shi et al. [15] found that the 28-day compressive strength of seawater-mixed concrete was increased by 22%, compared to that of the freshwater-mixed counterpart. Similarly, Taylor and Kuwairi [16] reported that the 28-day compressive strength of seawater-mixed concrete increased linearly with increasing seawater salinity from 0 to 7%. On the contrary, Younis et al. [17] and Mbadike et al.

[18] both indicated that the compressive strength of seawater-mixed concrete was lower than that of ordinary concrete. These apparent contradictions and complexities in experimental studies call for an atomic-level investigation of the fundamental role of seawater in cement pastes, especially considering that a cement paste undergoes a series of complex physical and chemical processes in its fresh and hardened states.

The macroscale material properties of concrete largely rely on the underlying mechanisms at smaller scales. Fig. 1 exhibits a schematic view of calcium silicate hydrate (C-S-H, the principal binding phase in concrete) in seawater-mixed concrete at the mesoscale and nanoscale. At the mesoscale, C-S-H gel exhibits a globular texture as revealed by atomic force microscopy imaging with the gel pores filled with a high concentration solution of salts.[10, 19] The interactions between C-S-H globules play a key role in the mechanical properties and durability (e.g. creep and shrinkage) of concrete.[20-24] From nanoscale insight, the interactions between C-S-H globules can be viewed as the interactions between two C-S-H layers interspersed with a layer filled with pore solution, which can be modeled through atomistic simulation.[25-27] In 2009, Pellenq et al. [28] proposed the first all-atom model of C-S-H by modifying the Hamid's tobermorite model. In recent years, atomistic simulations have been widely applied for investigating the physical and chemical properties of C-S-H gel. For example, Zhang et al. [29] studied the structure and mechanical properties of C-S-H gel, considering the influence of temperature. Hou et al. [30] simulated the capillary transport process of water in C-S-H pores of various sizes. Duque-Redondo et al. [31] and Jiang et al. [32] explored the adsorption and diffusion behaviors of different ions (Cs^+, Na^+, K^+, Ca^{2+}, Ba^{2+}, and Cl^-) in C-S-H gel, and Masoumi et al. [22] investigated the effective interactions of C-S-H nanolayers separated from each other by a layer of water. These atomic-level studies have facilitated a better understanding of the chemistry and physics of cement-based materials, which are usually not accessible through experimental approaches. However, to the best of the authors' knowledge, no atomic-level investigations have been carried out to explore the fundamental influence of seawater on the properties of C-S-H gel.

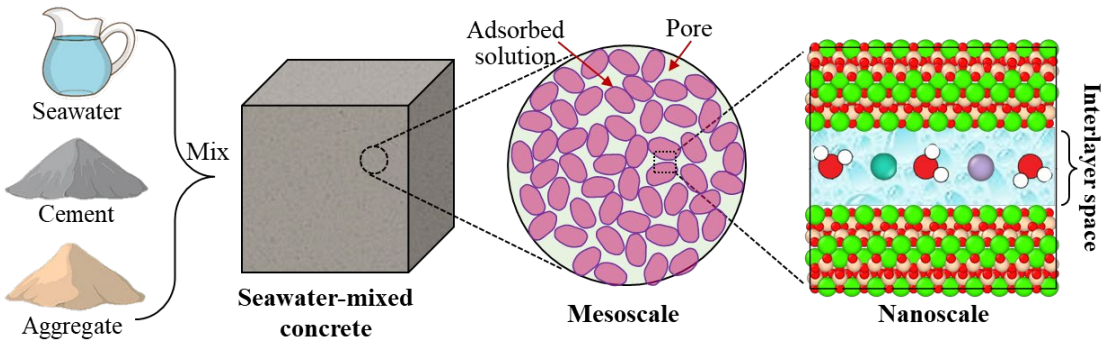

Fig. 1 Schematic view of the C-S-H binder gel in seawater-mixed concrete at the mesoscale and nanoscale. At the mesoscale, C-S-H gel exhibits a globular texture with the pores filled with a high concentration solution of salts. At the nanoscale, the interactions between two C-S-H globules can be described as the interactions between two C-S-H layers interspersed with a layer filled with NaCl solution.[33, 34]

In this study, atomistic simulations were performed to offer direct insights into the working mechanisms of seawater (using NaCl solutions) in C-S-H gel. The molecular structure of two C-S-H layers interspersed with a 5.0 Å space in between the two layers was created to establish the molecular models of C-S-H layered structures. The interlayer space was then filled with NaCl aqueous solutions to represent seawater, considering three different NaCl concentrations ($NaCl/H_2O$ mole ratios = 0.00, 0.05, and 0.10). While the cement pore solution has a high pH and other ions that affect the near surface composition and properties of the C-S-H gel, the goal here was to understand the direct effect of NaCl on the interaction between C-S-H globules. The atomic trajectories of Na^+ ions, Cl^- ions, H_2O molecules, and Ca^{2+} ions from the C-S-H layer surfaces were recorded to reveal the influence of Na^+ ions and Cl^- ions on the C-S-H layered structures. Next, a series of out-of-plane uniaxial tensile tests along the z-direction using the strain constant method was conducted to investigate the debonding behavior of the C-S-H layers. Finally, shear loading in the xy plane along the y-direction was applied to the C-S-H layered structures to observe the sliding behavior of the C-S-H layers, focusing on the influence of NaCl concentrations.

2. Computational Methods

2.1 Model construction

To construct the C-S-H layered models, a (6 × 5 × 1) supercell of the Hamid's monoclinic 11Å-tobermorite structure (6.69 Å × 7.39 Å × 22.77 Å, $\alpha = \beta = 90^{o}$, $\gamma = 123.49^{o}$) was first transformed into an orthogonal model (33.48 Å × 36.95 Å × 22.77 Å, $\alpha = \beta = \gamma = 90^{o}$) containing two C-S-H layers [35]. The C-S-H layers were composed of negatively charged calcium silicate layers with the Si-O^{-} surfaces charge-balanced by Ca^{2+} cations.[22, 36] Then an initial 18.0 Å interlayer space was created to separate the two C-S-H layers from each other. Setting such an initial value provided sufficient space for placing the interlayer solutions without causing improper interactions (i.e. close contact) between the C-S-H layers and the interlayer solutions. Fig. 2(a) shows a perspective view of the initial atomic backbone of the C-S-H layered structure with an 18.0 Å interlayer space. The resulting structure contained a total of 1800 atoms. Next, three different interlayer solutions were constructed with an 8.0 Å thickness to investigate the influence of different NaCl concentrations on the properties of the C-S-H layered structure, as shown in Fig. 2(b). The 8.0 Å thickness corresponded to a 5.0 Å thickness of interlayer space after equilibration as discussed in Section 3.1. The 5.0 Å interlayer space is in the distance range within which two C-S-H layers can interact with each other, corresponding to the situation where two C-S-H globules are in close contact at the mesoscale.[22, 36-38] The density of the three model aqueous solutions was 1.05, 1.07, and 1.08 g/cm^3, respectively, and the corresponding $NaCl/H_2O$ mole ratios of these solutions were 0.00, 0.05 and 0.10 respectively, which represented a reasonable range of NaCl concentrations found in the pore solution of seawater-mixed cement.[10, 16] The aqueous solutions were placed in the middle of the interlayer space. As a result, three different C-S-H layered models were constructed with the interlayer space filled with different NaCl solutions ($NaCl/H_2O$ = 0.00, 0.05, and 0.10). Fig. 2(c-e) shows a perspective view of these initial models of C-S-H layered structures.

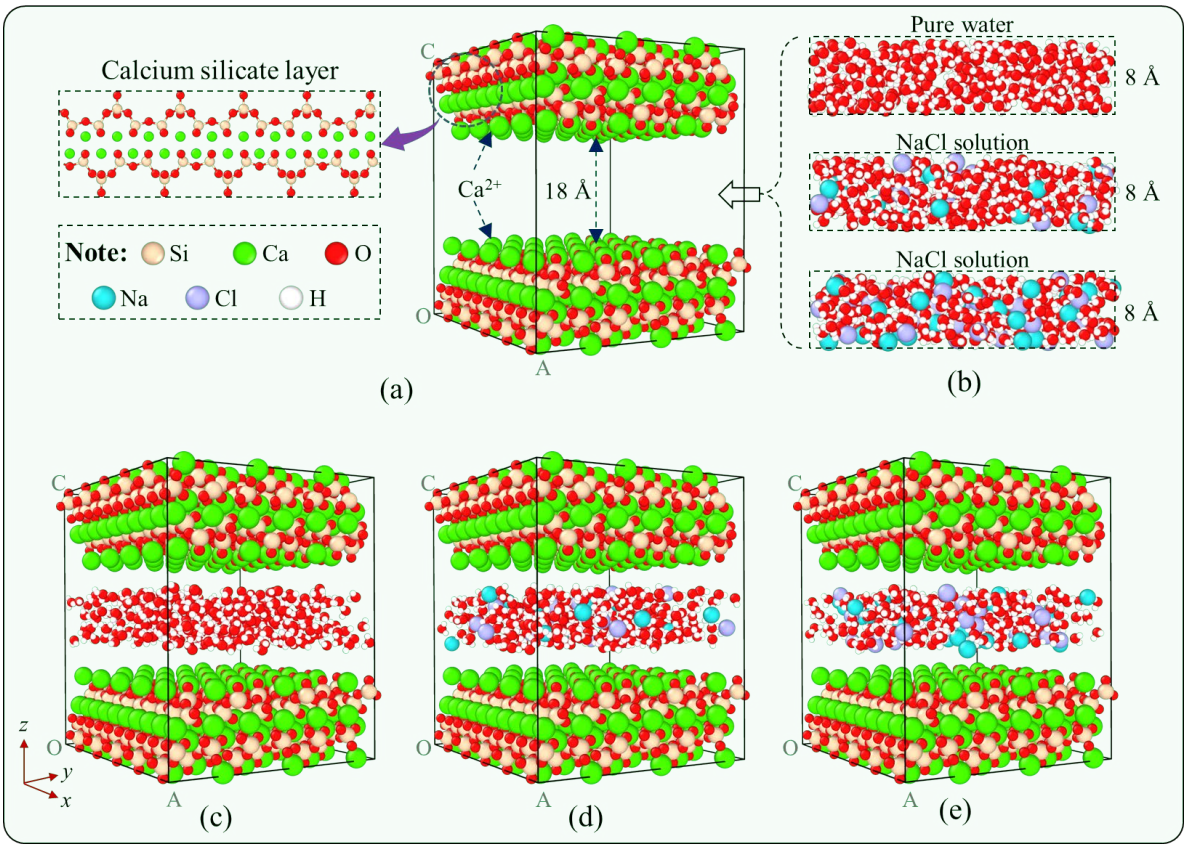

Fig. 2 Construction of the initial C-S-H layered models consisting of two C-S-H layers interspersed with a layer filled with different aqueous solutions: (a) A perspective view of the initial C-S-H atomic backbone (two C-S-H layers) with an 18.0 Å interlayer space; (b) Three different aqueous solutions with an 8.0 Å thickness to be placed into the middle of the interlayer space. The NaCl/H_2O mole ratios of these aqueous solutions are 0.00, 0.05, and 0.10 respectively; and (c-e) Perspective views of the initial C-S-H layered structures with the interlayer filled with the different aqueous solutions (NaCl/H_2O = 0.00, 0.05, and 0.10) before equilibration.

2.2 Force field

To describe the interatomic interactions in the C-S-H layered models, the empirical force field CSH-FF, specifically designed for C-S-H structures, was employed in this study. This force field is an updated version of the ClayFF force field.[39, 40] Generally, the total potential energy is comprised of Coulombic (electrostatic) interactions, van der Waals (vdW) interactions, and bonded interactions in water molecules,

$$E_{C-S-H} = E_{Coul} + E_{vdW} + E_{bond} + E_{angle} \quad (1)$$

where the bonded terms include the bond stretch and angle bend energy terms. To represent water, CSH-FF employs the flexible single point charge (SPC) water model, which considers the bond stretch term and angle bend term to be harmonic. Since CSH-FF does not include the parameters for Na^+ and Cl^- ions, the parameters from ClayFF for these two types of ions were added to CSH-FF to describe their interactions with other atoms,[41] as done in the literature.[31, 40, 42] The force field parameters employed in this study have been widely proven to be able to accurately study the performance of various aspects of C-S-H based systems, including the mechanical properties of C-S-H structure influenced by sodium/calcium cation exchange,[43] the diffusive behavior of solutions in porous C-S-H structures,[38] and alkali (Na^+, K^+, and Cs^+) adsorption on C-S-H surfaces.[40, 42] Different from Reactive force field (e.g., ReaxFF), CSH-FF is a non-reactive force field, which does not consider the potential chemical events as well as any charge transfer in a system.

2.3 Simulation details

First, the initial atom positions and cell dimensions were relaxed based on the energy minimization technique at 0 K and 0 kPa with a convergence criterion of 10^{-6} kcal/mol. Then the atomic structures were equilibrated for 250 ps under an isothermal-isobaric (NPT) ensemble. The Nose-Hoover thermostat and barostat algorithms were employed for the temperature (300 K) and pressure (101 kPa, atmospheric pressure) control.[44] Next, a heat treatment at 500 K for 2.5 ns was used to accelerate the dynamic equilibrium of the atomic structures,[45] followed by a quenching process (cooling rate = 10 K/ps) to cool the structures down to 300 K. Finally, a further dynamic equilibrium was carried out for another 250 ps under an NPT ensemble (300 K and 101 kPa). During the entire equilibrium process, the atom trajectories were recorded to observe the interactions between the C-S-H layers and the interlayer solutions.

To investigate the debonding behavior of the C-S-H layered structures under the influence of different interlayer solutions, a uniaxial tensile loading (σ_z) was applied to the equilibrated models along the z-direction. A constant-strain method (strain rate = 0.01%/ps) was employed for the loading scheme, which indicates that the cell dimension along the z-direction changed

linearly with the simulation time. The strain rate of 0.01%/ps is in the typical range of 1×10^{-2}/ps to 1×10^{-4}/ps suggested in the literature for atomistic simulations of mechanical tests.[34] Similarly, a shear loading (τ_{yz}) was applied to the equilibrated models using the constant-strain method (strain rate = 0.01%/ps) to cause the sliding of the C-S-H layers and investigate the influence of different interlayer solutions. For all the loading schemes mentioned above, an NPT ensemble (300 K and 101 kPa) was implemented to consider the potential Poisson effect.

All the simulations were performed using the Large-scale Atomic/Molecular Massively Parallel Simulator (LAMMPS) package with a time step of 0.25 fs. Periodic boundary conditions were applied to all directions of the structures during all the simulation processes mentioned above.

3. Results and Discussion

3.1 Structural analysis

During the dynamic equilibrium process, the adsorption from the interlayer solutions on the C-S-H layer surfaces was observed by recording the atom trajectories. The negatively-charged calcium silicate layers could adsorb both H_2O molecules and Na^+ ions from the interlayer solutions (Fig. 3a and b). Initially, the H_2O molecules in the interlayer solutions interacted with each other via hydrogen bonds (H-bonds), as shown in Fig. 3(a.1). Due to the hydrophilicity of the calcium silicate layers, the H_2O molecules could be adsorbed at different locations, as shown in Fig. 3(a.2−a.4). The H-bond number between one H_2O molecule and the C-S-H layers was either one or two, and the total H-bond number of one H_2O molecule was usually 4, which is typical for H_2O molecules.[46] Together with the H_2O molecules, the Na^+ ions in the interlayer solutions were adsorbed by the calcium silicate layers (Fig. 3b). Initially, the Na^+ ions in the interlayer solutions were coordinated mainly with the H_2O molecules and occasionally with the Cl^- ions, as shown in Fig. 3(b.1). During the dynamic equilibrium process, the Na^+ ions could coordinate with the oxygen (O) atoms of the layers due to electrostatic adsorption. The bond number between one Na^+ ion and the layers ranged from 1 to 3, as shown in Fig. 3(b.2−b.4). The charge-balancing Ca^{2+} ions that were tightly coordinated with the calcium silicate layers

could also adsorb the H_2O molecules via Ca–O_w bonds (O_w denotes the O from H_2O), as shown in Fig. 3(c.1). Interestingly, with the adsorption of the H_2O molecules and Na^+ ions on the surface of the calcium silicate layers, a few Ca^{2+} ions were found to be released from the surface, as shown in Fig. 3(c.2–c.4). The Ca–O_s bonds (O_s denotes the O from the layers) were gradually replaced by the Ca–O_w bonds, leading to the release of Ca^{2+} ions from the surface. In summary, the C-S-H layers interacted with the interlayer solution via H-bonds, Na–O_s bonds, and Ca–O_w bonds, and the interaction between the C-S-H layers and the NaCl solutions caused the release of a few Ca^{2+} ions from the C-S-H surface.

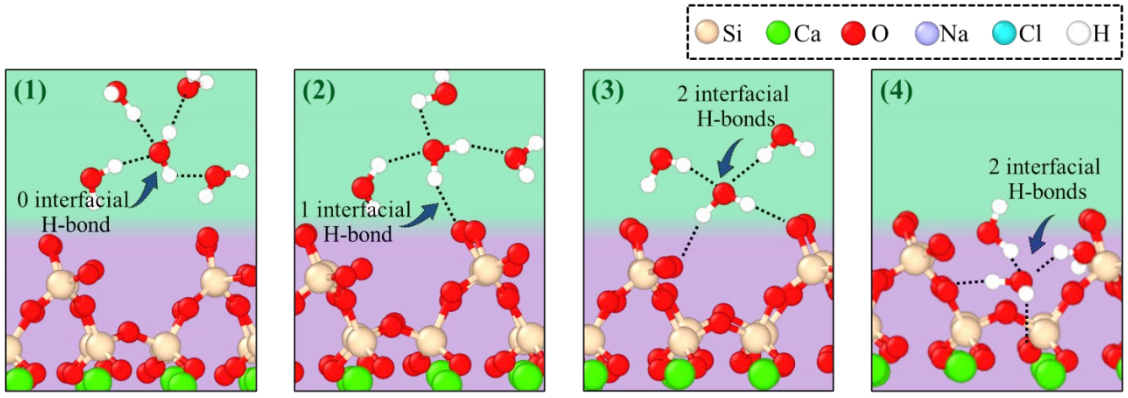

(a) The adsorption of H_2O on the surface of calcium silicate layers

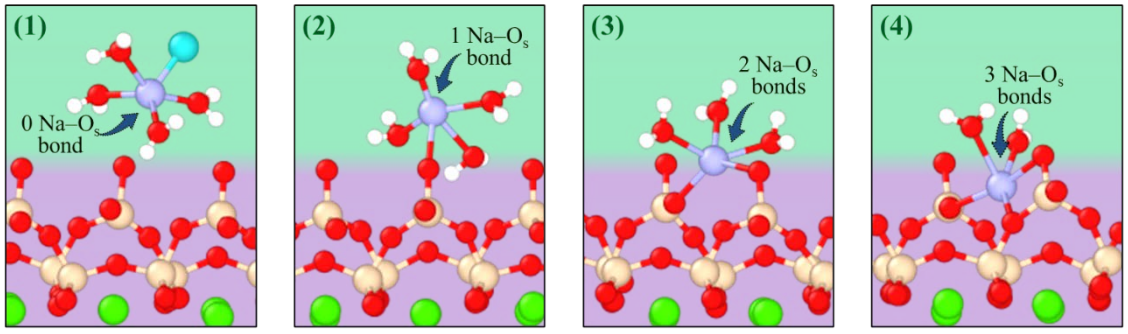

(b) The adsorption of Na^+ cations on the surface of calcium silicate layers

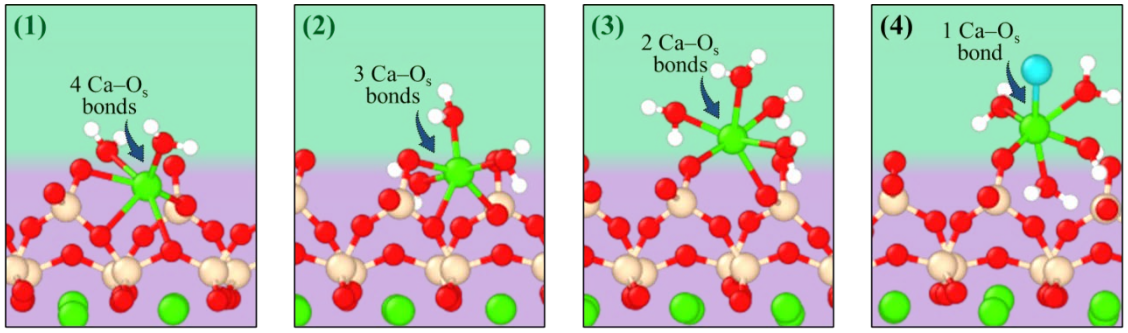

(c) The release of Ca^{2+} cations from the surface of calcium silicate layers

Fig. 3 Snapshots of the inter-atomic interactions between the C-S-H layers and the interlayer solutions: (a) absorption of H_2O molecules on the surface of calcium silicate layers; (b) adsorption of Na^+ ions on the surface of calcium silicate layers; and (c) release of Ca^{2+} ion from the C-S-H surface. The H-bond is defined according to the geometric criterion that characterizes two molecules to be hydrogen bonded if the O–O distance is separated by ⩽ 3.5 Å and the O–H···O angle is less than 30°.[46] The Ca–O bond was defined according to the geometric criterion that the O–O distance is separated by ⩽ 3.5 Å and the O–H···O angle is less than 30°. The Ca–O bond is defined when the Ca–O distance is shorter than 3.0 Å according to the criterion proposed by Hou et al. [47] based on the radial distribution function.

After the dynamic equilibrium, snapshots of the distribution of the Na^+ ions and Cl^- ions in the interlayer solutions and Ca^{2+} ions in the calcium silicate layers were taken, as shown in Fig. 4(a). Many Na^+ ions located at the surface of the C-S-H layers with different penetration depths due to electrostatic adsorption. In contrast, the Cl^- ions preferred to locate in the middle of the interlayer solutions. For the Ca^{2+} ions, most of them remained within the layers, while a few were found away from the layers. To reveal the influence of the NaCl concentrations on the bonding at the solid-solution interface, the variation of the bonds (including Na−O_s bond, H-bond and Ca−O_s bond) was determined**,** as shown in Fig. 4(b). The Na−O_s bond number at the solid-solution interface increased gradually with increasing NaCl concentration. It increased by ~ 49.3/nm^2 when the NaCl/H_2O mole ratio increased from 0.00 to 0.10. However, the H-bond number decreased by ~ 7.70/nm^2, due to the competition between the Na^+ ions and H_2O molecules for the O_s of the layers. In addition, the increasing NaCl concentrations led to the loss of Ca−O_s bonds on the surface of the calcium silicate layers, and ~ 1.02/nm^2 Ca−O_s bonds were lost with the NaCl/H_2O mole ratio increasing from 0.00 to 0.10. The increasing number of Na−O_s bonds was ~ 5−6 times the lost number of Ca−O_s bonds, which indicated that the Na^+ absorption capacity was much larger than the Ca^{2+} release capacity. The results demonstrated that there existed an Na−Ca cation exchange between the C-S-H layers and the NaCl solutions, which is a common phenomenon observed in experiments.[43, 48] In conclusion, the Na^+ ions showed a strong adsorption capacity on the calcium silicate layers, which can cause the partial

release of Ca^{2+} ions from the surface (termed as "Na−Ca cation exchange"). Increasing NaCl concentration led to more Na−Ca cation exchange as well as the loss of H-bond at the solid-solution interface.

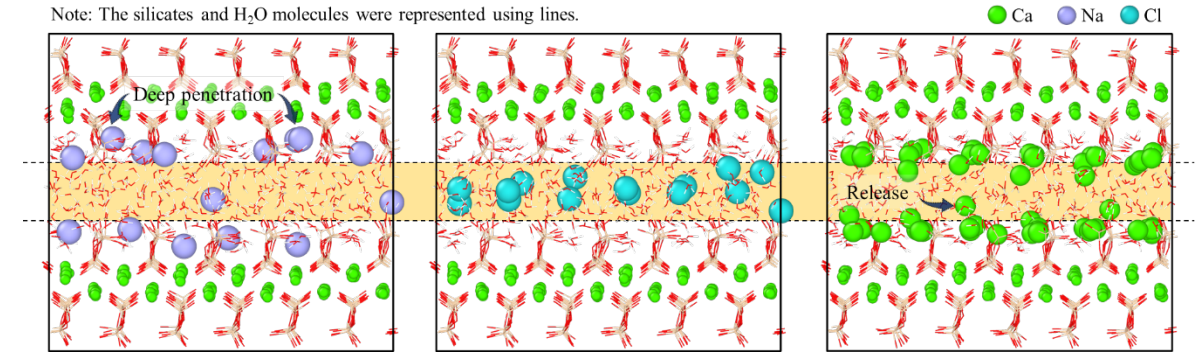

(a) Distribution of Na^+, Cl^- and Ca^{2+} ions

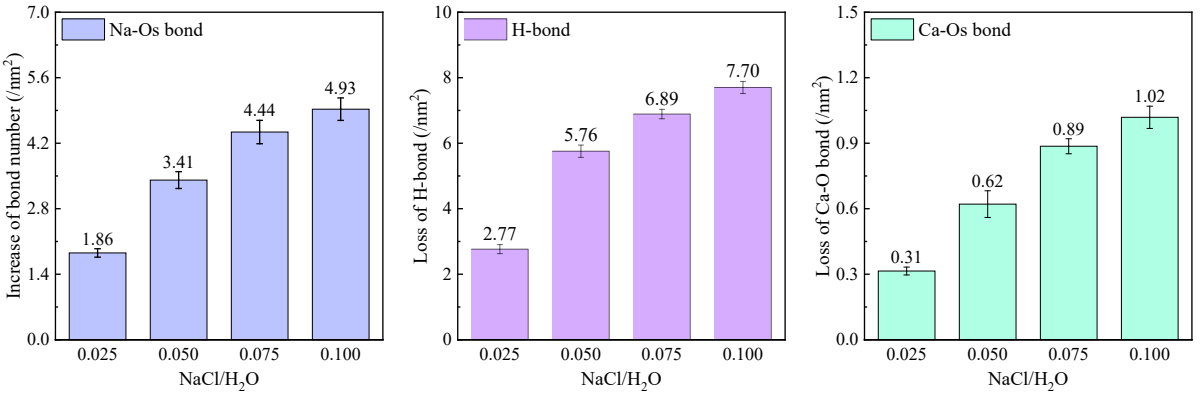

(b) Variation of interfacial bonds

Fig. 4 (a) Snapshots of the distribution of Na^+, Cl^- and Ca^{2+} ions in the C-S-H layered structures ($NaCl/H_2O$ = 0.05). The dash lines represent the surface lines (where the O of $Si{-}O^-$ locates) of the calcium silicate layers, which can be used to observe the penetration depth of Na^+; and (b) Variation of the interfacial bonds (the values were normalized using the surface area of C-S-H), including the $Na{-}O_s$ bond, H-bond, and $Ca{-}O_s$ bond. Note: to better reveal the influence of NaCl concentrations on the variation of the interfacial bond, two more cases ($NaCl/H_2O$ = 0.25 and 0.75) are shown.

Based on the findings above, Fig. 5 shows a schematic view of the Na−Ca cation exchange between NaCl solution and C-S-H gel. When the solution was NaCl rather than water, the interfaces between the solution and the C-S-H layers were in a non-equilibrium state. It was

because the Ca^{2+} ions on the C-S-H surface were the concentrated charge points and each Ca^{2+} balanced several negatively charged O atoms exposed on the surface, which means that the exposed O atoms were more than the Ca^{2+} in quantity on the C-S-H surface. Therefore, the O atoms that were not fully coordinated by cations had the potential to adsorb more cations (i.e., Na^{+}) from the solutions, leading to the C-S-H surface being over-charged. As a result, the confinement (electrostatic adsorption) of the C-S-H surface on the Ca^{2+} became weaker, thus in the thermodynamics process, the Ca^{2+} ions had more possibility to leave from the C-S-H surface. Similar results leading to a positively-charged surface that can further absorb anions at the outer layer have been reported by Bourg et al. [49] for the adsorption of cations from electrolyte (NaCl–$CaCl_2$) solutions by smectite surfaces. Burgos et al. [50] also found that NaCl solutions in pores of quartz can result in an over-charged surface of the quartz.

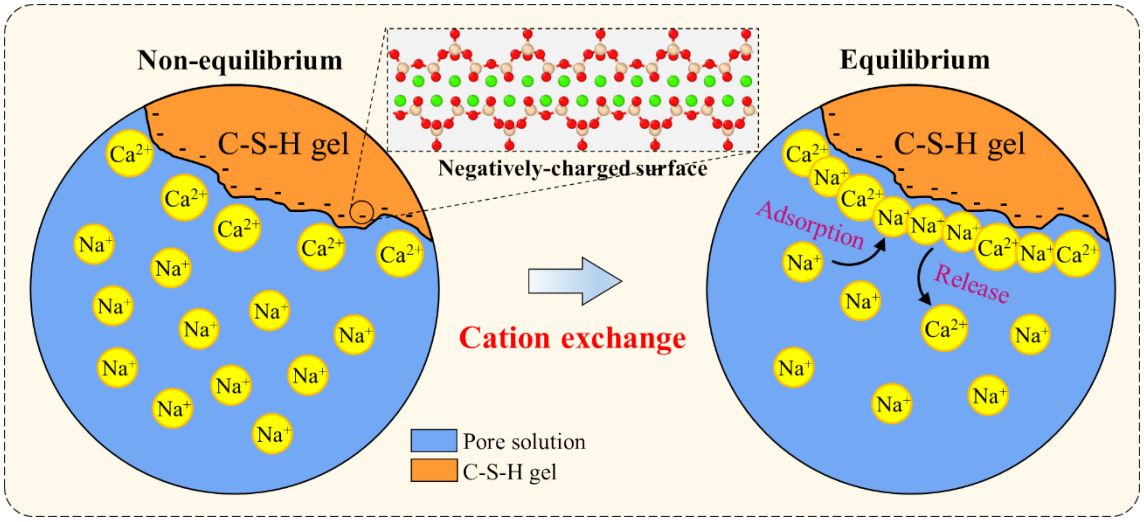

Fig. 5 A schematic view of the Na−Ca cation exchange between NaCl solution and C-S-H gel. Initially, the negative-charged surface is charge-balanced by Ca^{2+} ions, but the surface is in a non-equilibrium state. At the equilibrium state, many Na^{+} ions from the solution are adsorbed on the C-S-H surface, while a few Ca^{2+} ions are released from the surface, which is termed as "Na−Ca cation exchange."

To further understand the influence of seawater on the C-S-H layered structures, the atomic density profiles of the C-S-H layers (including the calcium silicate layers and the Ca^{2+} ions from the C-S-H layer surfaces) and interlayer solutions were plotted (Fig. 6) as a function of

distance along the z-direction. Due to the semi-crystalline character of the calcium silicate layers, different peaks corresponding to the position of different atom types could be observed (Fig. 6(a)), and the position of the surface line where the O of the $Si{-}O^{-}$ of the calcium silicate layers locates could be characterized. The distance between the surface lines of the two layers, defined as the width of the interlayer space,[51, 52] was 5.0 Å for the three different C-S-H layered structures, which satisfied the design requirement to keep the interlayer space constant for different interlayer solutions. The three density profiles of the calcium silicate layers were almost the same, suggesting that the variation of NaCl concentrations did not significantly influence the structure of the calcium silicate layers. Fig. 6(b) shows the atomic density profiles of the Ca^{2+} ions of the C-S-H layers. For the C-S-H layered structure with $NaCl/H_2O = 0.00$ (Fig. 6(b.1)), the two peaks at z = 11.6 Å and 18.1 Å (corresponding to the Ca^{2+} ions on the wet C-S-H layer surfaces) were wider than the other two peaks at z = 1.6 Å and 28.1 Å (corresponding to the Ca^{2+} ions on the dry C-S-H layer surfaces), indicating that the water molecules weakened the tight-bonding of Ca^{2+} ions of the C-S-H layer surfaces. With the increase in NaCl concentrations (Fig. 6(b.2) and (b.3)), the Ca^{2+} ions at the solid-solution interfaces distributed over a wider range, and the average z-coordinate of these Ca^{2+} ions moved away from the C-S-H surface towards the interlayer, which was consistent with the previous findings that a few Ca^{2+} ions were released from the surface due to the presence of NaCl. Fig. 6(c) shows the atomic density profiles of the interlayer solutions for different NaCl concentrations. The total width of the different interlayer solutions remained at ~ 12.5 Å. This width was larger than the width of the interlayer space (5.0 Å) because of the filling of the H_2O molecules and ions into the molecular voids at the surface of the C-S-H layers, as illustrated in Fig. 3 and Fig 4(a). In addition, the density in the middle zone of the interlayer solution increased gradually with increasing NaCl concentration, which was attributed to the accumulation of Cl^{-} ions in this zone, as shown in Fig 4(a). In conclusion, the increase in NaCl concentration of the interlayer solutions caused two effects: (1) a wider distribution range of Ca^{2+} ions at the surface of the C-S-H layers due to the release of Ca^{2+} ions, and (2) a higher density in the middle of the interlayer solution due to the accumulation of Cl^{-} ions in this zone.

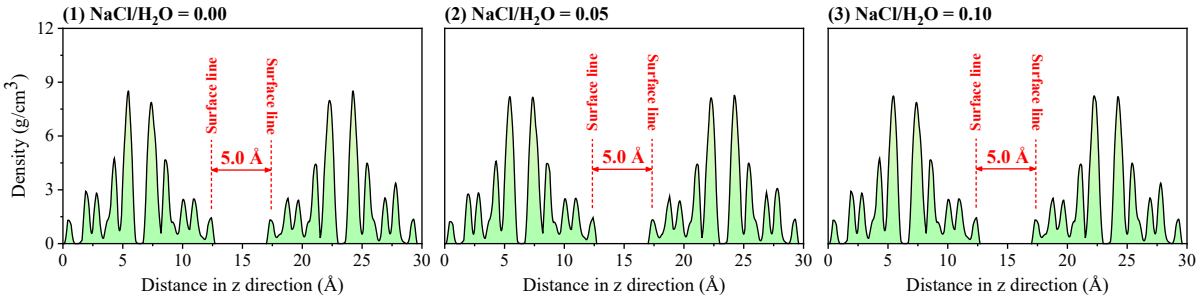

(a) Density profiles of the calcium silicate layers

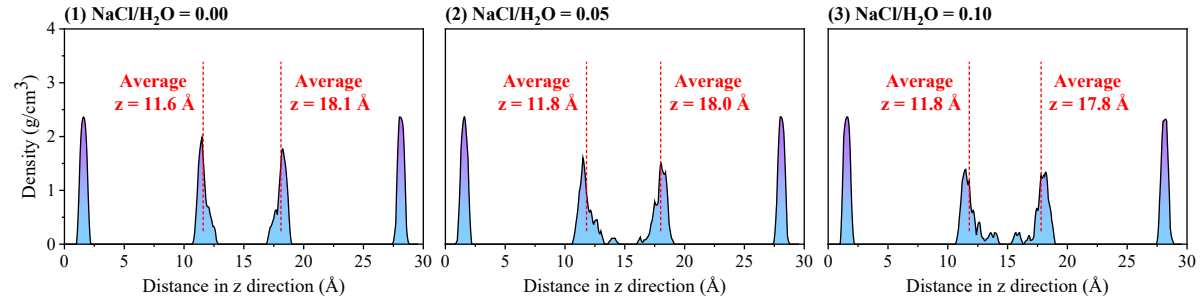

(b) Density profiles of the Ca^{2+} ions of the C-S-H layers

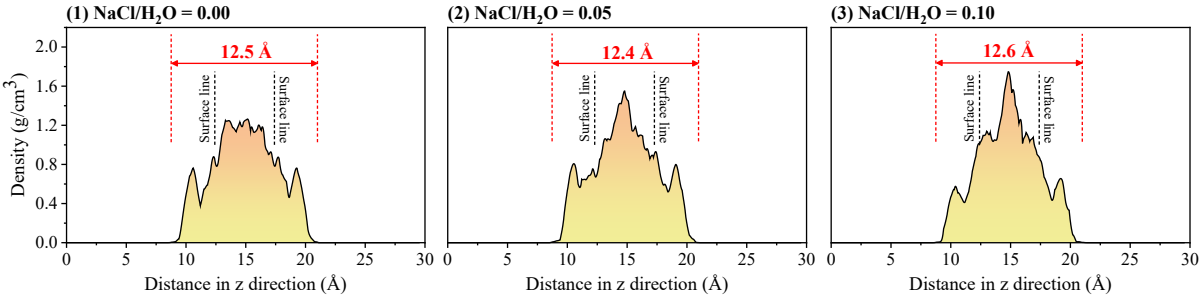

(c) Density profiles of the interlayer solutions

Fig. 6 Atomic density profiles of the C-S-H layered structures made of different interlayer solutions ($NaCl/H_2O$ = 0.00, 0.05, and 0.10): (a) density profiles of the calcium silicate layers (the dash lines represent the surface lines where the O of the $Si{-}O^-$ of the calcium silicate layers locates); (b) Density profiles of Ca^{2+} ions of the C-S-H layers (the dash lines label the average z-position of the Ca^{2+} ions from each C-S-H surface); (c) Density profiles of the interlayer solutions.

3.2 Debonding behavior

The debonding between C-S-H layers at the atomic level, which corresponds to the debonding between C-S-H globules at the mesoscale, is one of the most noteworthy features that play an important role in the mechanical and fracture properties of C-S-H gel.[24, 53]

Therefore, a series of tensile loading along the z-direction was carried out on the C-S-H layered structures made of different interlayer solutions ($NaCl/H_2O$ = 0.00, 0.05, and 0.10) in order to investigate the role of seawater in the debonding process. First, the tensile stress (P_z) was calculated using the following equation during the debonding process,[34]

$$P_z = \frac{\sum_k^N m_k v_{k_z} v_{k_z}}{V} + \frac{\sum_k^{N'} r_{k_z} f_{k_z}}{V} \quad (2)$$

where N denotes the number of atoms in the system; V denotes the system volume; m_k is the mass of the k^{th} atom; v_{k_z} is the component in the z-direction of the velocity of the k^{th} atom; N' includes the atoms from the neighboring sub-domains (so-called "ghost atoms"); r_{k_z} and f_{k_z} are the component in z-direction of the position and force of the k^{th} atom.

Fig. 7(a) presents the stress-strain curves of the C-S-H layered structures made of different interlayer solutions during tensile loading along the z-direction. For all structures, the tensile stress increased linearly with the tensile strain (the elastic stage) and then reached a maximum peak, after which the tensile stress decreased gradually with the further increase in tensile strain (the fracture stage). The Young's modulus of the C-S-H layered structures, determined by calculating the slope of the curves at the elastic stage, was 37.9, 40.1, and 41.2 GPa for the three structures, respectively. The bond strength (peak stress) between the two C-S-H layers was 1.03, 1.19 and 1.32 GPa, respectively. At the fracture stage, the tensile stress at a given strain (e.g. 10% and 15% strain, as shown in Fig. 7a) was also higher with increasing NaCl concentration. The results indicated that the bond between the two C-S-H layers was enhanced by increasing the NaCl concentration. Furthermore, the strain value at the peak became larger, from 4.5%. to 5.5%, indicating that increasing the NaCl concentration delayed the occurrence of fracture of the C-S-H layered structure. In addition, the system potential energy (i.e. sum of the interaction energy of all atoms in a system) was recorded during the debonding process, as shown in Fig. 7(b). Before tensile loading, the potential energy of the three structures was -410,539, -412,724, and -414,669 kcal/mol respectively, indicating that increasing NaCl concentration caused a decrease (more negative) in the system potential energy. In other words, the total atomic interactions in the structures were enhanced by increasing the NaCl concentration of the

interlayer solution. During the debonding process, the system potential energy increased gradually (less negative) and then reached a plateau. The maximum change in the system potential energy was 559, 603, and 630 kcal/mol respectively for the three different C-S-H layered structures. With increasing NaCl concentration in the interlayer solution, more energy was needed to overcome the atomic interactions during the debonding process. In conclusion, increasing the NaCl concentration of the interlayer solution (1) enhanced the bond performance between the C-S-H layers, (2) delayed the occurrence of fracture of the C-S-H layered structure, and (3) required more energy during the debonding process.

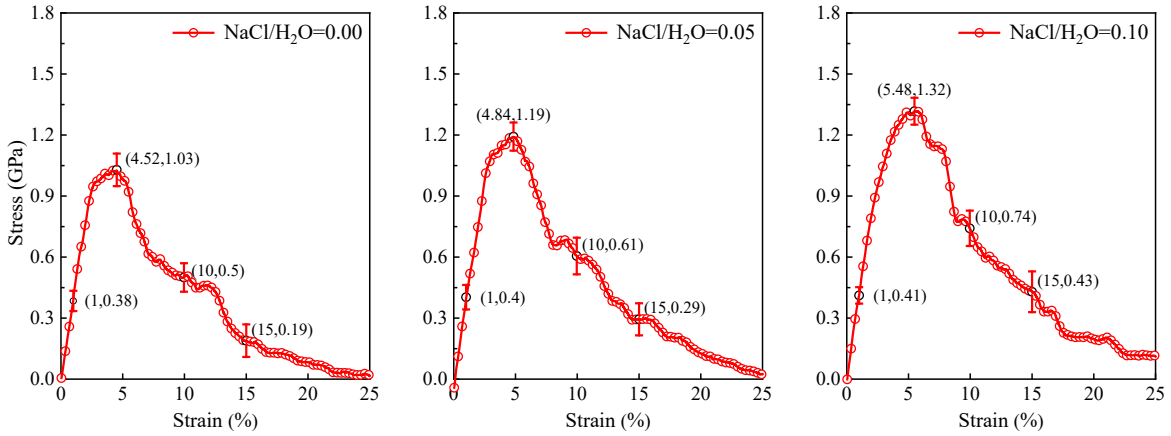

(a) Stress-strain curves

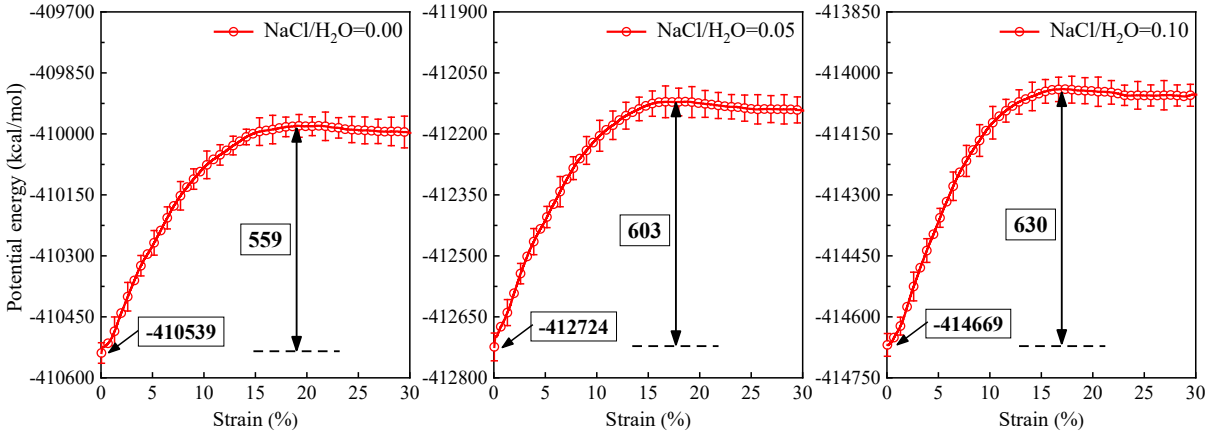

(b) System potential energy

Fig. 7 (a) Tensile stress-strain curves for the C-S-H layered structures made of different interlayer solutions ($NaCl/H_2O$ = 0.00, 0.05, and 0.10); and (b) System potential energy of the C-S-H layered structures made of different interlayer solutions ($NaCl/H_2O$ = 0.00, 0.05, and 0.10) as a function of tensile strain.

To understand the influence of seawater on the fracture mechanisms of the C-S-H layered structures, the fracture process of two C-S-H layered structures ($NaCl/H_2O$ = 0.00 and 0.10 for the interlayer solutions) was recorded. Fig. 8(a) and (b) show snapshots of the two structures at 10%, 20% and 30% strains. At strain = 10%, the crack initiated at the interlayer solution, suggesting that the interatomic interactions within the solutions were weaker than those at the solid-solution interface due to the strong hydrophilicity of C-S-H layers. At strain = 20%, the crack propagated nearly through the entire interlayer solution, leaving only a few atoms bridging the upper and lower layers. By observing the local structures of these atoms (Fig.8c), it could be seen that in the layered structure with $NaCl/H_2O$ = 0.00 for the interlayer solution, a few H_2O molecules formed a chain to bridge the upper and lower layers. These H_2O molecules interacted with each other via H-bonds, while the chain end bridged the C-S-H layers via H-bond or Ca−O ionic bond. For the layered structure with $NaCl/H_2O$ = 0.10 for the interlayer solution, the chain was composed of H_2O molecules, Na^+ ions and Cl^- ions, and thus the chain involved H-bond, Na−O ionic bond, and Cl−H ionic bond. The chain end bridged the C-S-H layers via H-bond, Ca−O ionic bond, or Na−O ionic bond. It is widely reported in the literature that atomic chain bridging contributes to the residual strength of materials.[44, 47, 54] At strain = 30%, the chains broke and thus the two C-S-H layers were completely debonded. Fig.8 (d)) and (e) show the density profiles of two C-S-H layered structures ($NaCl/H_2O$ = 0.00 and 0.10 for the interlayer solutions) at different strains (10%, 20% and 30%). It is clear that the density of the middle region of the solution deceased gradually during the tensile process, and finally the interlayer solutions were separated equally to the two surfaces of the C-S-H layers, which agreed well with the fracture process shown in Fig. 8(a) and (b). In conclusion, the fracture process of the C-S-H layered structures underwent three stages: (i) crack propagation in the interlayer solution, (ii) atomic chain bridging between the C-S-H layers, and (iii) complete debonding of the C-S-H layers. After introducing NaCl into the interlayer solutions, both Na^+ and Cl^- ions were involved in the H_2O chain bridging, which may have contributed to the residual bond strength.

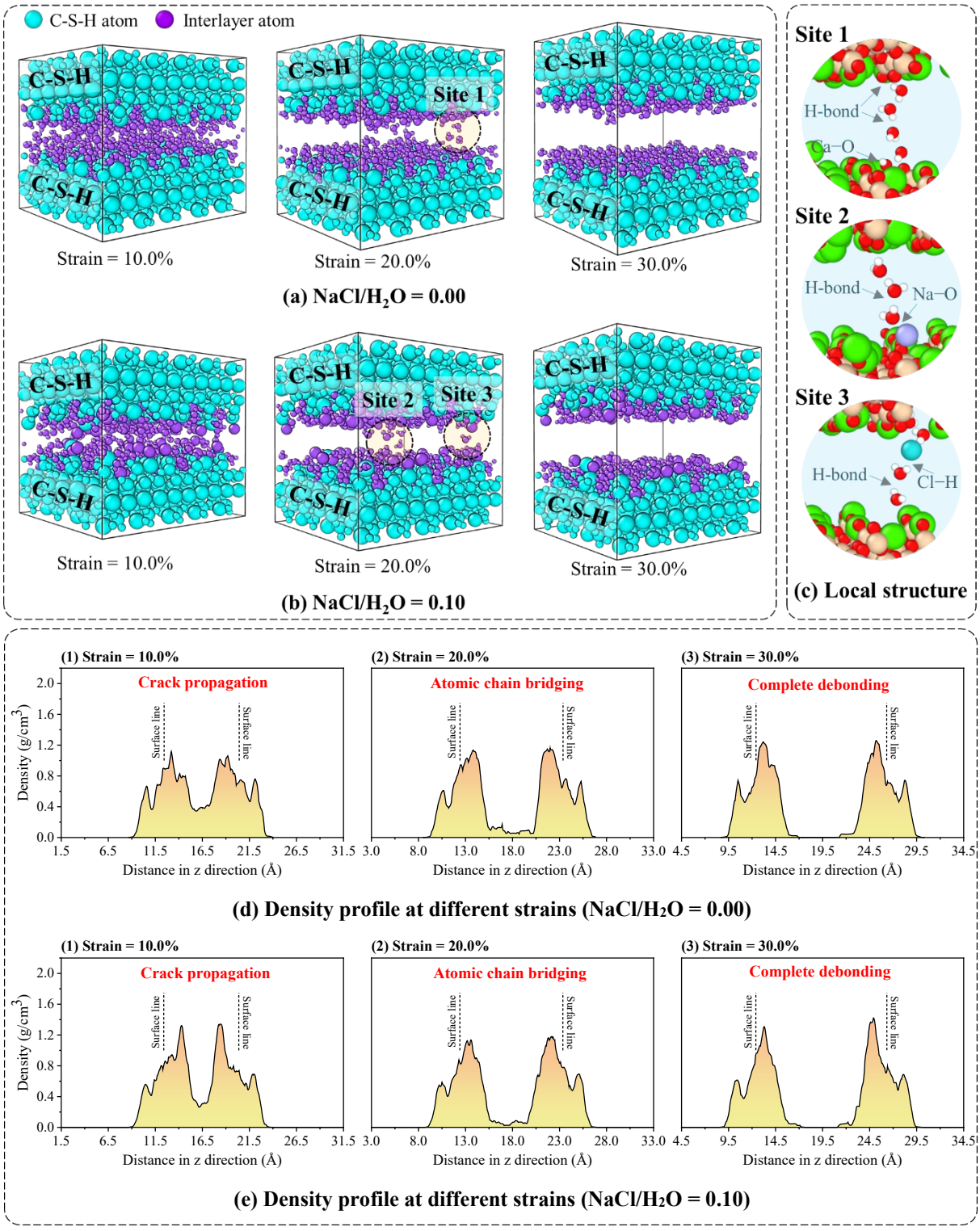

Fig. 8 Fracture process of the C-S-H layered structures with two different interlayer solutions: (a) snapshots of the structure (NaCl/H2O = 0.00); (b) snapshots of the structure (NaCl/H2O = 0.10). The black circles are used to label the sites where chain bridging was formed between the two C-S-H layers; (c) local structures at the sites where the atomic chain bridging was formed (the color assigned to the atoms is the same as that in Fig. 1); (d and e) density profile of the interlayer solution (NaCl/H_2O = 0.00 and 0.10) at different strains (10%, 20% and 30%).

To gain a deeper insight into how seawater influenced the bond performance of C-S-H layered structures, the atomic stresses of the H_2O molecules, Na^+ ions and Cl^- ions in the interlayer solutions were calculated to reveal their contribution to the stress transfer in the system. The bond strength between the two C-S-H layers of the C-S-H layered structures was the combined result of the direct interactions between the two C-S-H layers and the stress transfer via the interlayer solution.[34] Since the interlayer space was the same for all layered structures, the direct interactions between the two C-S-H layers during the debonding process could be considered the same and is therefore not further discussed. To study the stress transfer capacity of the interlayer solutions, the atomic stress (σ_i) of the H_2O molecules, Na^+ ions and Cl^- ions in the interlayer solutions was calculated in the form of virial stress using the following equation:

$$\sigma_i = \frac{1}{V_i}\left[-m_i\vec{v}_i \otimes \vec{v}_i + \frac{1}{2}\sum_{j\neq i}^{N}(\vec{r}_{ij} \otimes \vec{F}_{ij})\right] \quad (3)$$

where m_i and $\vec{v}_i$ represent the mass and velocity vectors of the i^{th} atom; $\vec{r}_{ij} = \vec{r}_i - \vec{r}_j$ is the relative position of atom i in relation to atom j; $\vec{F}_{ij}$ is the force acting upon atom i due to interaction with atom j; the symbol $\otimes$ represents the cross product operator; and V_i is the atomic volume based on the Voronoi analysis.[55]

Fig. 9(a) shows the atomic stress of the H_2O molecules, Na^+ ions, and Cl^- ions in the C-S-H layered structure with $NaCl/H_2O = 0.10$ for the interlayer solution. For the H_2O molecules, the atomic stress was negative before tensile loading, which indicated that the H_2O molecules were under compression. With the increase in tensile strain, the atomic stress increased gradually until the peak stress was reached, at which point the atomic stress turned positive, indicating that the H_2O molecules were then under tension and thus contributed to the transfer of the tensile stress. For the Na^+ ions, the atomic stress was positive before tensile loading, which indicated that the Na^+ ions were under tension. With the increase in tensile strain, the atomic stress increased gradually until the peak stress, which indicated that the Na^+ ions also contributed to the transfer of the tensile stress. Furthermore, the increase rate of the atomic

stress for the Na^+ ions was ~ 3 times that of the H_2O molecules, indicating that the stress transfer capacity of Na^+ was much greater than that of the H_2O molecules. For the Cl^- ions, the atomic stress was negative before tensile loading and the Cl^- ions were under compression. With the increase in tensile strain, the atomic stress increased gradually and then reached a plateau, but remained always negative during the entire tensile loading. This result indicated that the tensile process only led to the release of the compressive stress of the Cl^- ions, and thus that the Cl^- ions did not contribute to the transfer of the tensile stress.

To further understand the different stress transfer capacities of the H_2O molecules, Na^+ ions and Cl^- ions in the interlayer solutions, the per-atom potential for the H_2O molecules, Na^+ ions and Cl^- ions was calculated, as shown in Fig. 9(b). Overall, the per-H_2O potential and per-Na^+ potential increased gradually until reaching their peaks, indicating that the H_2O molecules and Na^+ ions contributed to resist the tensile load. The maximum increase of the per-H_2O potential and per-Na^+ potential was respectively 0.79 kcal/mol and 2.44 kcal/mol, indicating that the contribution of Na^+ ions to resist the tensile load was much greater than that of H_2O molecules. For Cl^- ions, however, the per-Cl^- potential decreased gradually until reaching a plateau. The decrease of the per-Cl^- potential indicated that the debonding process led to the release of compressive stress of the Cl^- ions. Therefore, it can be concluded that the Na^+ ions had much greater stress transfer capacity than the H_2O molecules, which is why the introduction of NaCl into the interlayer solution can enhance the bond strength of the C-S-H layered structures. In contrast, the Cl^- ions did not contribute to enhancing the bond strength.

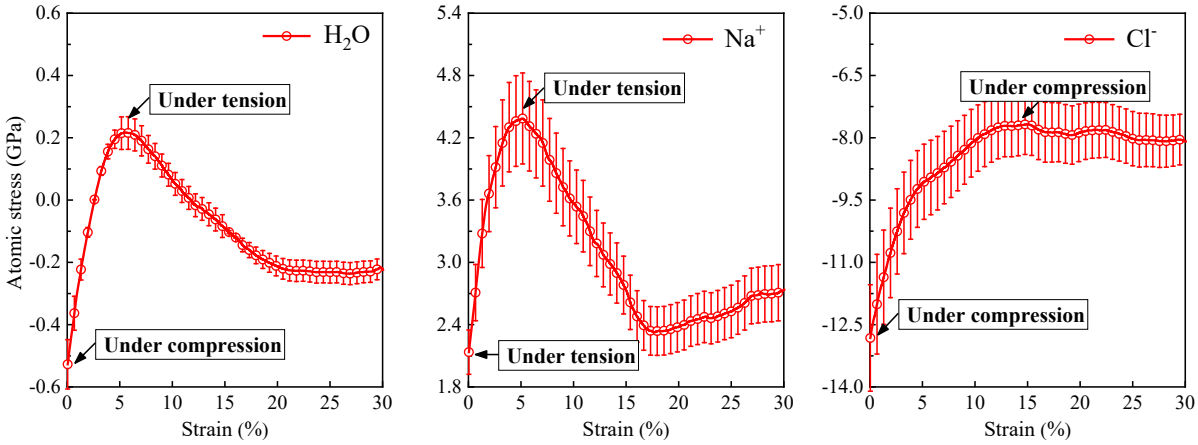

(a) Atomic stress

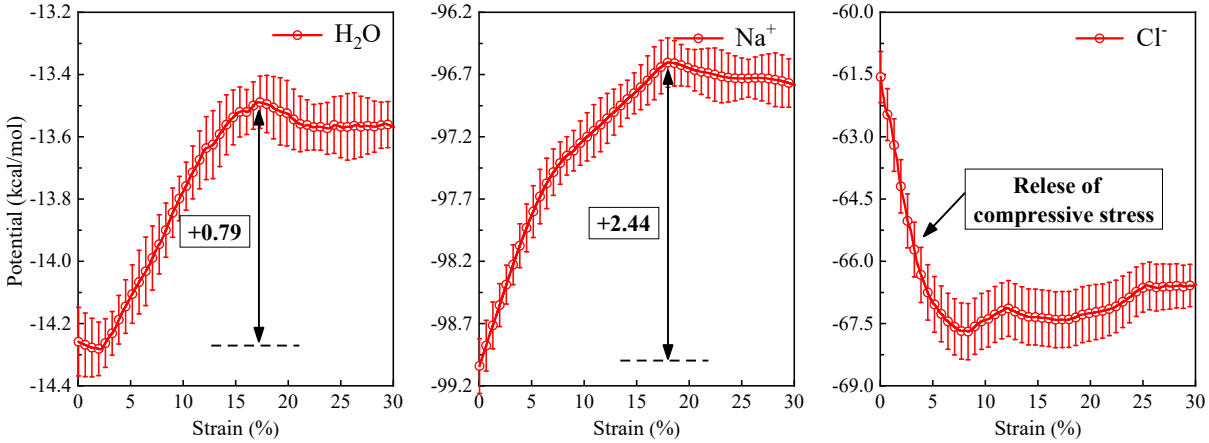

(b) Per-atom potential

Fig. 9 (a) Atomic stress of the H_2O molecules, Na^+ ions and Cl^- ions of the C-S-H layered structure with NaCl/H_2O = 0.10 for the interlayer solution; (b) Per-atom potential for the H_2O molecules, Na^+ ions, and Cl^- ions of the C-S-H layered structure with NaCl/H_2O = 0.10 for the interlayer solution.

3.3 Sliding behavior

The sliding behavior of C-S-H layers at the atomic level, which corresponds to the sliding between C-S-H globules at the mesoscale, is another important feature that plays a key role in both the short-term and long-term properties (e.g. creep) of C-S-H gel.[26, 33, 56] Therefore, a series of shear loads (τ_{yz}) was applied to the C-S-H layered structures made of different interlayer solutions (NaCl/H_2O = 0.00, 0.05, and 0.10) to study the sliding of C-S-H layers. Fig. 10(a) illustrates the three deformed C-S-H layered structures under shear loading in the xy plane along the y axis. By recording the atom displacement along the y axis of the deformed structures, the origin of shear deformation can be understood, as shown in Fig. 10(b). For all the deformed structure, there is a negligible shear deformation in the two C-S-H layers (the solid part) and the deformation only arises from the interlayer solution (the liquid part). In other words, the shear loading caused sliding of C-S-H layers over each other with the interlayer solutions acting as lubricant. This result was consistent with results reported in the literature by Morshedifard et al. [26] for the sliding behavior between two C-S-H layers based on the all-atom topological analysis. In addition, for the layered structure with NaCl/H_2O = 0.00 as the interlayer solution

(Fig. 10(b.1)), most of the Ca^{2+} ions on the C-S-H layer surfaces remained tightly bonded to the layers during the deformation process. However, after introducing NaCl into the interlayer solution, a few Ca^{2+} ions moved over the C-S-H surface, as labelled in Fig. 10(b.2−b.3). This further indicated that a few Ca^{2+} ions had a weak bond strength with the layers due to the presence of NaCl in the interlayer solution, which was consistent with the previous finding of the release of Ca^{2+} ions from the C-S-H surface.

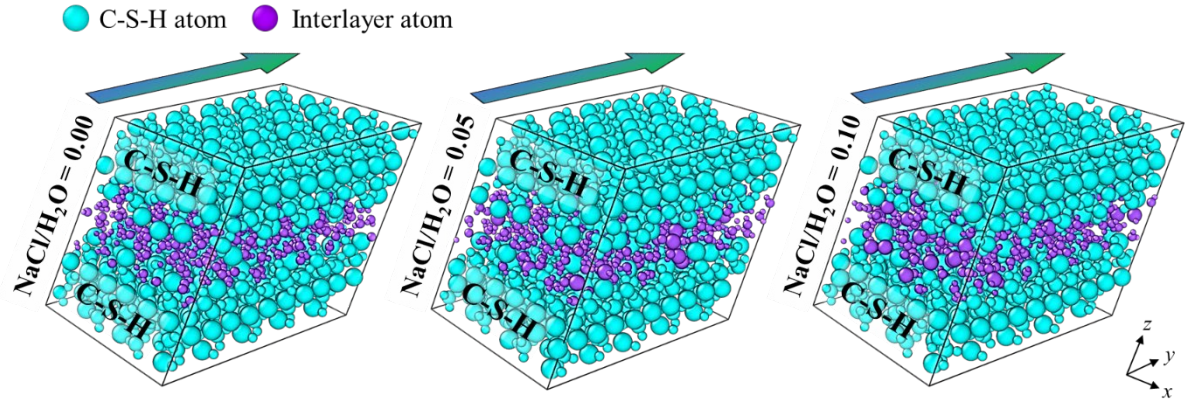

(a) Deformed C-S-H layered structures

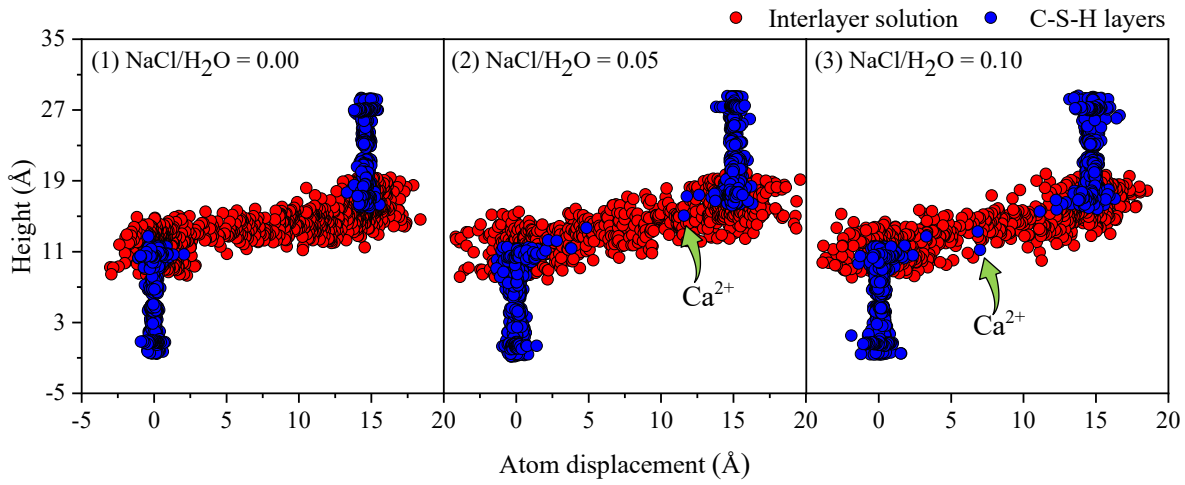

(b) Atom displacement along the y-direction

Fig. 10 (a) Deformed C-S-H layered structures made of different interlayer solutions ($NaCl/H_2O$ = 0.00, 0.05, and 0.10) at 50% shear strain; and (b) Atom displacement along y-direction of the C-S-H layers and the interlayer solution ($NaCl/H_2O$ = 0.00, 0.05, and 0.10) of the C-S-H structures at 50 % shear strain.

Fig. 11 shows the shear stress-strain curves of the C-S-H layered structures made of different interlayer solutions ($NaCl/H_2O$ = 0.00, 0.05, and 0.10). Overall, the shear stress of the three structures had a linear relationship with the shear strain during the initial stage (elastic stage) of the loading. After reaching a maximum value, the shear stress fluctuated with peaks and valleys around a mean shear stress as the strain further increased. The maximum peak shear stress was 0.29, 0.35, and 0.42 GPa for the three C-S-H layered structures, respectively and the mean shear stress at the fluctuation stage was 0.14, 0.26, and 0.36 GPa, respectively. These results indicated that the shear performance was enhanced by increasing NaCl concentration in the interlayer solution. Since the shear deformation of C-S-H layered structures originated from the sliding of the C-S-H layers over each other, it could be concluded that the sliding resistance between the C-S-H layers was enhanced by introducing NaCl into the interlayer solutions. In other words, the lubrication effect of the interlayer solution was reduced after introducing NaCl into the interlayer solutions.

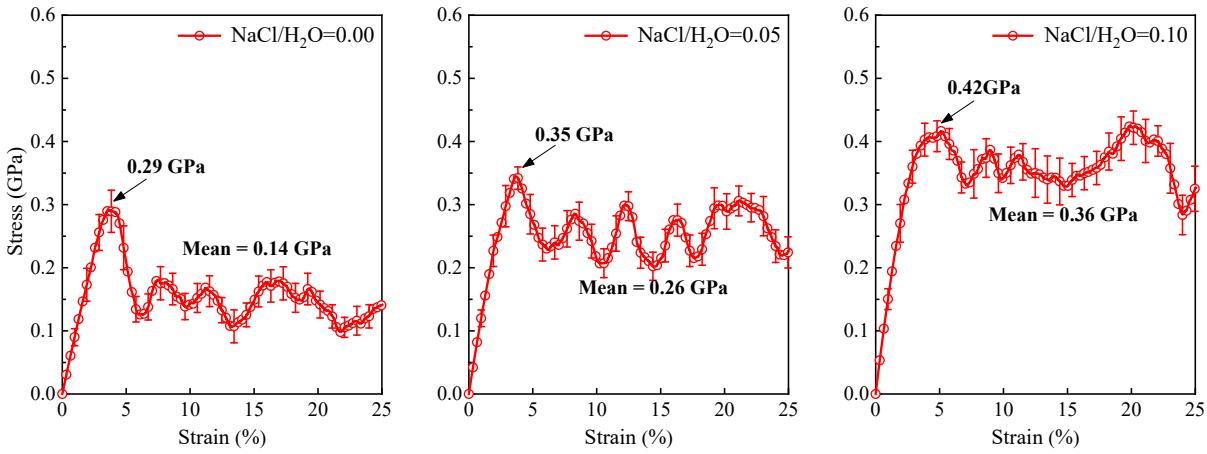

Fig. 11 Shear stress-strain curves of the C-S-H layered structures made of different interlayer solutions ($NaCl/H_2O$ = 0.00, 0.05, and 0.10).

To explain the influence of NaCl concentration on the sliding resistance between the C-S-H layers, two factors that play important roles in the sliding behaviors were investigated: one is the viscosity of the interlayer solution (the lubricant) [57-59] and the other is the interfacial adhesion between the C-S-H layers and the lubricant.[33, 60, 61] At the atomic level, the viscosity

of a liquid is the quantity that describes the resistance of the molecules to transport, which therefore has a reciprocal relationship with the diffusion ability of the molecules.[33, 62] In this study, the diffusion coefficient (D) of the interlayer solutions was calculated to reveal the diffusion ability of the interlayer solutions, following the equation below,[44]

$$D = \frac{1}{6}\lim_{t\to\infty}\frac{\langle|\boldsymbol{r}(t)-\boldsymbol{r_0}|^2\rangle}{t} \approx \frac{1}{6N}\frac{\sum_{k=1}^{N}|\boldsymbol{r}_k(t_1)-\boldsymbol{r}_k(0)|^2}{t_1-t_0} \quad (4)$$

where N is the number of atoms to be averaged; vector $\boldsymbol{r}_i(t_1)$ is the position of the k^{th} atom at time t_1; vector $\boldsymbol{r}_i(0)$ is the reference position of the k^{th} atom at time t_0. Fig. 12a shows the diffusion coefficient of the interlayer solutions ($NaCl/H_2O$ = 0.00, 0.05, and 0.10) as a function of distance along the z-direction. For all interlayer solutions, the diffusion coefficient increased gradually with the distance and reached a maximum in the middle of the interlayer solution, after which it decreased with a further increase of the distance in the z-direction. The results indicated that the diffusion of the interlayer solutions was faster the further away from the surfaces of the C-S-H layers. The overall diffusion coefficients for the three interlayer solutions were 1.13, 0.90, and 0.78 $Å^2$/ns respectively, indicating that the introduction of NaCl into the interlayer solutions decreased the diffusion coefficient. In addition, please note that the diffusion coefficient of the confined solutions was much lower than that (319. 33, 207.24, and 137.44 $Å^2$/ns, respectively) of the bulk solutions. In conclusion, the viscosity of the interlayer solution was enhanced by the presence of NaCl in the interlayer solution, which had an adverse effect to the lubricating role of the solutions.[63] This result agreed with experimental data from the literature that indicates that the viscosity of NaCl solutions at room temperature decreases with increasing NaCl concentration.[64]

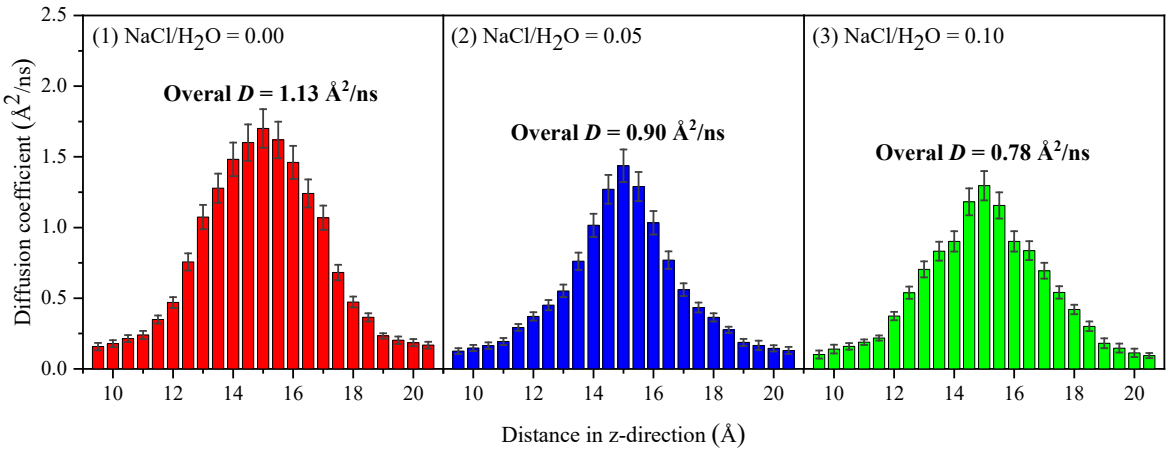

(a) Diffusion coefficients of the interlayer solutions

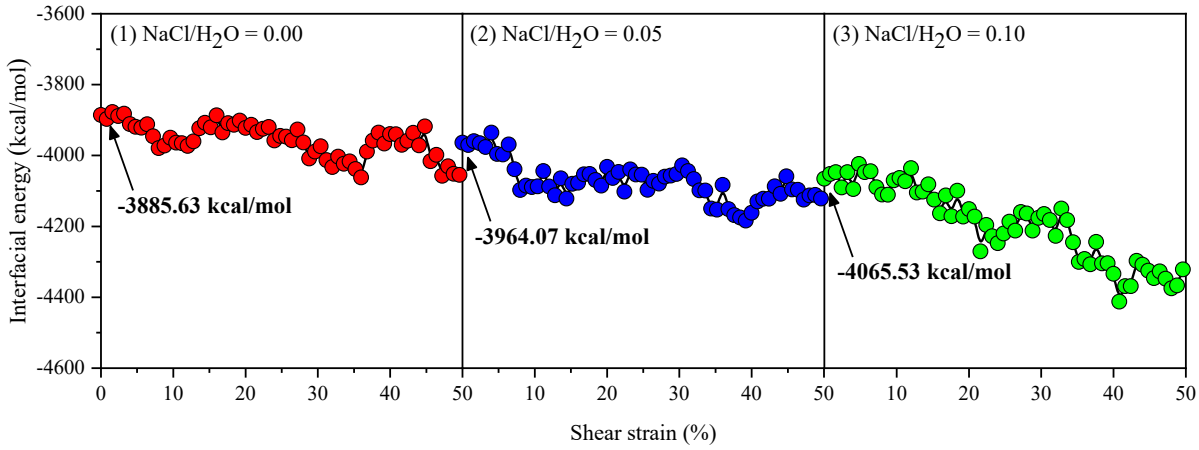

(b) Interfacial interaction energy

Fig. 12 (a) Diffusion coefficients of the interlayer solutions ($NaCl/H_2O$ = 0.00, 0.05, and 0.10) as a function of distance in z-direction. For the calculation of diffusion coefficients, the interlayer solution was cut into small 0.5 Å-thick regions along z-direction. The diffusion coefficients of each region were obtained using Eq. (4). The atom positions over a timescale of 500 ps were recorded for the calculation; (b) Variation of the interfacial interaction energy between the C-S-H layers and the interlayer solutions under shear loading.

To reveal the effect of NaCl concentration on the interfacial adhesion between the C-S-H layers and the interlayer solutions, the interfacial interaction energy was calculated using the following equation:

$$E_{Interface} = E_{System} - E_{Layers} - E_{Solution} \quad (5)$$

where E_{System} is the total potential energy of the layered structure, E_{Layers} is the potential energy of the two C-S-H layers and $E_{Solution}$ is the potential energy of the interlayer solution.

Fig. 12(b) shows the variation of the interfacial interaction energy between the C-S-H layers and the interlayer solutions as a function of shear strain. The initial interfacial interaction energy for the three structures was ca. -3885, -3964, and -4065 kcal/mol, respectively. Lower interfacial interaction energy (more negative) corresponds to a stronger interfacial adhesion.[33] Therefore, the results showed that the interfacial adhesion was strengthened by increasing NaCl concentrations in the interlayer solution. Furthermore, the interfacial interaction energy slightly decreased during the sliding process, which was attributed to the fact that the sliding process could overcome some energy barriers to optimize the atom positions.

Therefore, it can be concluded that increasing NaCl concentration can increase the viscosity of the interlayer lubricant and strengthen the interfacial adhesion between the C-S-H layers and the lubricant, both of which are unfavourable to the lubrication effect of the interlayer solution. This explains why the sliding resistance between the C-S-H layers was enhanced after introducing NaCl into the interlayer solution.

4. Conclusions

In this work, molecular models of two C-S-H layers interspersed with NaCl solutions of different concentrations ($NaCl/H_2O$ = 0.00, 0.05, and 0.10) were constructed. The following conclusions can be drawn from the atomistic simulations:

(1) Thermodynamically, the Na^+ ions of the interlayer solutions showed a strong adsorption capacity onto the C-S-H layer surfaces, which caused partial release of Ca^{2+} ions from the C-S-H layer surfaces (termed as "Na−Ca cation exchange") into the interlayer solutions. Increasing NaCl concentration in the interlayer solution led to more Na−Ca cation exchanges and the loss of H-bond at the solid-solution interface.

(2) The bond performance between the C-S-H layers was enhanced by introducing NaCl into the interlayer solution. The bond strength increased from 0.97 to 1.36 GPa when the $NaCl/H_2O$ mole ratio increased from 0.00 to 0.10 as a result of Na^+ ions having a greater stress transfer capacity than the H_2O molecules. Cl^- ions, however, did not enhance the bond performance.

(3) The occurrence of fracture of the C-S-H layered structure was delayed by introducing NaCl into the interlayer solutions. Overall, the fracture process underwent three stages: crack propagation through the interlayer solution, atomic chain bridging between the C-S-H layers, and complete debonding of the C-S-H layers. After introducing NaCl into the interlayer solution, both Na^+ and Cl^- ions were involved in the H_2O chain bridging, which may have contributed to the residual bond strength.

(4) Under shear loading, the C-S-H layers slid over each other with the interlayer solutions acting as lubricant. The sliding resistance between the C-S-H layers was enhanced by the presence of NaCl in the interlayer solutions. The following two mechanisms responsible for the enhanced sliding resistance were identified: (1) NaCl increased the viscosity of the interlayer lubricant and (2) the solid-solution interface was strengthened by introducing NaCl into the interlayer solution.

Declaration of competing interest

The authors declare that they have no known competing financial interests or personal relationships that could have appeared to influence the work reported in this paper.

Acknowledgments

This research was supported by the Hong Kong Research Grants Council—Theme-based Research Scheme (Project code: T22-502/18-R), Guangdong Province R&D Plan for Key Areas (Project code: 2019B111107002), and the NSFC/RGC Joint Research Scheme (Project code: N_PolyU542/20).

References

1. Miller, S. A.; Horvath, A.; Monteiro, P. J., Impacts of booming concrete production on water resources worldwide. *Nature Sustainability* **2018,** *1* (1), 69-76.

2. Ebead, U.; Lau, D.; Lollini, F.; Nanni, A.; Suraneni, P.; Yu, T., A review of recent advances in the science and technology of seawater-mixed concrete. *Cement and concrete research* **2022,** *152*, 106666.

3. Huang, B.-T.; Wu, J.-Q.; Yu, J.; Dai, J.-G.; Leung, C. K.; Li, V. C., Seawater sea-sand engineered/strain-hardening cementitious composites (ECC/SHCC): Assessment and modeling of crack characteristics. *Cement and Concrete Research* **2021,** *140*, 106292.

4. Sun, Y.; Lu, J.-X.; Poon, C. S., Strength degradation of seawater-mixed alite pastes: an explanation from statistical nanoindentation perspective. *Cement and Concrete Research* **2022,** *152*, 106669.

5. Wang, J.; Liu, E.; Li, L., Multiscale investigations on hydration mechanisms in seawater OPC paste. *Construction and Building Materials* **2018,** *191*, 891-903.

6. Li, P.; Li, W.; Sun, Z.; Shen, L.; Sheng, D., Development of sustainable concrete incorporating seawater: A critical review on hydration, microstructure and mechanical strength. *Cement and Concrete Composites* **2021**, 104100.

7. Zhao, Y.; Hu, X.; Shi, C.; Zhang, Z.; Zhu, D., A review on seawater sea-sand concrete: Mixture proportion, hydration, microstructure and properties. *Construction and Building Materials* **2021,** *295*, 123602.

8. Montanari, L.; Suraneni, P.; Tsui-Chang, M.; Khatibmasjedi, M.; Ebead, U.; Weiss, J.; Nanni, A., Hydration, pore solution, and porosity of cementitious pastes made with seawater. *Journal of Materials in Civil Engineering* **2019,** *31* (8), 04019154.

9. Yaseen, S. A.; Yiseen, G. A.; Poon, C. S.; Li, Z., Influence of seawater on the morphological evolution and the microchemistry of hydration products of tricalcium silicates (C3S). *ACS Sustainable Chemistry & Engineering* **2020,** *8* (42), 15875-15887.

10. Li, P.; Li, W.; Yu, T.; Qu, F.; Tam, V. W., Investigation on early-age hydration, mechanical properties and microstructure of seawater sea sand cement mortar. *Construction and Building Materials* **2020,** *249*, 118776.

11. Sikora, P.; Lootens, D.; Liard, M.; Stephan, D., The effects of seawater and nanosilica on the performance of blended cements and composites. *Applied Nanoscience* **2020,** *10* (12), 5009-5026.

12. Guo, M.; Hu, B.; Xing, F.; Zhou, X.; Sun, M.; Sui, L.; Zhou, Y., Characterization of the mechanical properties of eco-friendly concrete made with untreated sea sand and seawater based on statistical analysis. *Construction and Building Materials* **2020,** *234*, 117339.

13. Li, Q.; Geng, H.; Huang, Y.; Shui, Z., Chloride resistance of concrete with metakaolin addition and seawater mixing: A comparative study. *Construction and Building Materials* **2015,** *101*, 184-192.

14. Li, Q.; Geng, H.; Shui, Z.; Huang, Y., Effect of metakaolin addition and seawater mixing on the properties and hydration of concrete. *Applied Clay Science* **2015,** *115*, 51-60.

15. Shi, Z.; Shui, Z.; Li, Q.; Geng, H., Combined effect of metakaolin and sea water on performance and microstructures of concrete. *Construction and Building Materials* **2015,** *74*, 57-64.

16. Taylor, M. A.; Kuwairi, A., Effects of ocean salts on the compressive strength of concrete. *Cement and Concrete Research* **1978,** *8* (4), 491-500.

17. Younis, A.; Ebead, U.; Suraneni, P.; Nanni, A., Fresh and hardened properties of seawater-mixed concrete. *Construction and Building Materials* **2018,** *190*, 276-286.

18. Mbadike, E.; Elinwa, A., Effect of salt water in the production of concrete. *Nigerian Journal of Technology* **2011,** *30* (2), 105-110.

19. Nonat, A., The structure and stoichiometry of CSH. *Cement and concrete research* **2004,** *34* (9), 1521-1528.

20. Qomi, M. J. A.; Brochard, L.; Honorio, T.; Maruyama, I.; Vandamme, M., Advances in atomistic modeling and understanding of drying shrinkage in cementitious materials. *Cement and Concrete Research* **2021,** *148*, 106536.

21. Haist, M.; Divoux, T.; Krakowiak, K. J.; Skibsted, J.; Pellenq, R. J.-M.; Müller, H. S.; Ulm, F.-J., Creep in reactive colloidal gels: A nanomechanical study of cement hydrates. *Physical Review Research* **2021,** *3* (4), 043127.

22. Masoumi, S.; Zare, S.; Valipour, H.; Abdolhosseini Qomi, M. J., Effective interactions between calcium-silicate-hydrate nanolayers. *The Journal of Physical Chemistry C* **2019,** *123* (8), 4755-4766.

23. Bonnaud, P. A.; Labbez, C.; Miura, R.; Suzuki, A.; Miyamoto, N.; Hatakeyama, N.; Miyamoto, A.; Van Vliet, K. J., Interaction grand potential between calcium–silicate–hydrate nanoparticles at the molecular level. *Nanoscale* **2016,** *8* (7), 4160-4172.

24. Hou, D.; Zhang, W.; Wang, P.; Wang, M.; Zhang, H., Mesoscale insights on the structure, mechanical performances and the damage process of calcium-silicate-hydrate. *Construction and Building Materials* **2021,** *287*, 123031.

25. Dupuis, R.; Moon, J.; Jeong, Y.; Taylor, R.; Kang, S.-H.; Manzano, H.; Ayuela, A.; Monteiro, P. J.; Dolado, J. S., Normal and anomalous self-healing mechanism of crystalline calcium silicate hydrates. *Cement and Concrete Research* **2021,** *142*, 106356.

26. Morshedifard, A.; Masoumi, S.; Qomi, M. A., Nanoscale origins of creep in calcium silicate hydrates. *Nature communications* **2018,** *9* (1), 1-10.

27. Hou, D.; Jia, Y.; Yu, J.; Wang, P.; Liu, Q., Transport properties of sulfate and chloride ions confined between calcium silicate hydrate surfaces: a molecular dynamics study. *The Journal of Physical Chemistry C* **2018,** *122* (49), 28021-28032.

28. Pellenq, R. J.-M.; Kushima, A.; Shahsavari, R.; Van Vliet, K. J.; Buehler, M. J.; Yip, S.; Ulm, F.-J., A realistic molecular model of cement hydrates. *Proceedings of the National Academy of Sciences* **2009,** *106* (38), 16102-16107.

29. Zhang, Y.; Zhou, Q.; Ju, J. W.; Bauchy, M., New insights into the mechanism governing the elasticity of calcium silicate hydrate gels exposed to high temperature: A molecular dynamics study. *Cement and Concrete Research* **2021,** *141*, 106333.

30. Hou, D.; Zhang, W.; Sun, M.; Wang, P.; Wang, M.; Zhang, J.; Li, Z., Modified Lucas-Washburn function of capillary transport in the calcium silicate hydrate gel pore: A coarse-grained molecular dynamics study. *Cement and Concrete Research* **2020,** *136*, 106166.

31. Duque-Redondo, E.; Yamada, K.; Manzano, H., Cs retention and diffusion in CSH at different Ca/Si ratio. *Cement and Concrete Research* **2021,** *140*, 106294.

32. Liu, Z.; Xu, D.; Gao, S.; Zhang, Y.; Jiang, J., Assessing the adsorption and diffusion behavior of multicomponent ions in saturated calcium silicate hydrate gel pores using molecular dynamics. *ACS Sustainable Chemistry & Engineering* **2020,** *8* (9), 3718-3727.

33. Kai, M. F.; Zhang, L. W.; Liew, K. M., New insights into creep characteristics of calcium silicate hydrates at molecular level. *Cement and Concrete Research* **2021,** *142*, 106366.

34. Kai, M. F.; Zhang, L. W.; Liew, K. M., Atomistic insights into structure evolution and mechanical property of calcium silicate hydrates influenced by nuclear waste caesium. *Journal of Hazardous Materials* **2021,** *411*, 125033.

35. Tang, S.; Hubao, A.; Chen, J.; Yu, W.; Yu, P.; Chen, E.; Deng, H.; He, Z., The interactions between water molecules and CSH surfaces in loads-induced nanopores: A molecular dynamics study. *Applied Surface Science* **2019,** *496*, 143744.

36. Honorio, T., Monte Carlo molecular modeling of temperature and pressure effects on the interactions between crystalline calcium silicate hydrate layers. *Langmuir* **2019,** *35* (11), 3907-3916.

37. Masoumi, S.; Valipour, H.; Abdolhosseini Qomi, M. J., Intermolecular forces between nanolayers of crystalline calcium-silicate-hydrates in aqueous medium. *The Journal of Physical Chemistry C* **2017,** *121* (10), 5565-5572.

38. Duque-Redondo, E.; Masoero, E.; Manzano, H., Nanoscale shear cohesion between cement hydrates: The role of water diffusivity under structural and electrostatic confinement. *Cement and Concrete Research* **2022,** *154*, 106716.

39. Shahsavari, R.; Pellenq, R. J.-M.; Ulm, F.-J., Empirical force fields for complex hydrated calcio-silicate layered materials. *Physical Chemistry Chemical Physics* **2011,** *13* (3), 1002-1011.

40. Dufresne, A.; Arayro, J.; Zhou, T.; Ioannidou, K.; Ulm, F.-J.; Pellenq, R.; Béland, L. K., Atomistic and mesoscale simulation of sodium and potassium adsorption in cement paste. *The Journal of Chemical Physics* **2018,** *149* (7), 074705.

41. Cygan, R. T.; Liang, J.-J.; Kalinichev, A. G., Molecular models of hydroxide, oxyhydroxide, and clay phases and the development of a general force field. *The Journal of Physical Chemistry B* **2004,** *108* (4), 1255-1266.

42. Arayro, J.; Dufresne, A.; Zhou, T.; Ioannidou, K.; Ulm, J.-F.; Pellenq, R.; Béland, L. K., Thermodynamics, kinetics, and mechanics of cesium sorption in cement paste: A multiscale assessment. *Physical Review Materials* **2018,** *2* (5), 053608.

43. Yaphary, Y. L.; Lau, D.; Sanchez, F.; Poon, C. S., Effects of sodium/calcium cation exchange on the mechanical properties of calcium silicate hydrate (CSH). *Construction and Building Materials* **2020,** *243*, 118283.

44. Kai, M.-F.; Dai, J.-G., Understanding geopolymer binder-aggregate interfacial characteristics at molecular level. *Cement and Concrete Research* **2021,** *149*, 106582.

45. Abdolhosseini Qomi, M.; Krakowiak, K.; Bauchy, M.; Stewart, K.; Shahsavari, R.; Jagannathan, D.; Brommer, D. B.; Baronnet, A.; Buehler, M. J.; Yip, S., Combinatorial molecular optimization of cement hydrates. *Nature communications* **2014,** *5* (1), 1-10.

46. Luzar, A.; Chandler, D., Effect of environment on hydrogen bond dynamics in liquid water. *Physical review letters* **1996,** *76* (6), 928.

47. Hou, D.; Ma, H.; Zhu, Y.; Li, Z., Calcium silicate hydrate from dry to saturated state: Structure, dynamics and mechanical properties. *Acta materialia* **2014,** *67*, 81-94.

48. Bernard, E.; Yan, Y.; Lothenbach, B., Effective cation exchange capacity of calcium silicate hydrates (CSH). *Cement and Concrete Research* **2021,** *143*, 106393.

49. Bourg, I. C.; Sposito, G., Molecular dynamics simulations of the electrical double layer on smectite surfaces contacting concentrated mixed electrolyte (NaCl–CaCl2) solutions. *Journal of colloid and interface science* **2011,** *360* (2), 701-715.

50. Burgos, J. C.; Quiñones-Bolaños, E.; Saghir, M. Z.; Mehrvar, M., Seawater Transport through Quartz Pores of Coastal Aquifers: A Molecular Dynamics Study. *Advances in Water Resources* **2022**, 104121.

51. Deng, H.; He, Z., Interactions of sodium chloride solution and calcium silicate hydrate with different calcium to silicon ratios: A molecular dynamics study. *Construction and Building Materials* **2021,** *268*, 121067.

52. Wang, P.; Qiao, G.; Zhang, Y.; Hou, D.; Zhang, J.; Wang, M.; Wang, X.; Hu, X., Molecular dynamics simulation study on interfacial shear strength between calcium-silicate-hydrate and polymer fibers. *Construction and Building Materials* **2020,** *257*, 119557.

53. Yaphary, Y. L.; Sanchez, F.; Lau, D.; Poon, C. S., Mechanical properties of colloidal calcium-silicate-hydrate gel with different gel-pore ionic solutions: A mesoscale study. *Microporous and Mesoporous Materials* **2021,** *316*, 110944.

54. Hou, D.; Zhang, J.; Li, Z.; Zhu, Y., Uniaxial tension study of calcium silicate hydrate (C–S–H): structure, dynamics and mechanical properties. *Materials and structures* **2015,** *48* (11), 3811-3824.

55. Krishnan, N. A.; Wang, B.; Falzone, G.; Le Pape, Y.; Neithalath, N.; Pilon, L.; Bauchy, M.; Sant, G., Confined water in layered silicates: the origin of anomalous thermal expansion behavior in calcium-silicate-hydrates. *ACS Applied Materials & Interfaces* **2016,** *8* (51), 35621-35627.

56. Liu, H.; Dong, S.; Tang, L.; Krishnan, N. A.; Masoero, E.; Sant, G.; Bauchy, M., Long-term creep deformations in colloidal calcium–silicate–hydrate gels by accelerated aging simulations. *Journal of Colloid and Interface Science* **2019,** *542*, 339-346.

57. Briscoe, W. H., Aqueous boundary lubrication: Molecular mechanisms, design strategy, and terra incognita. *Current Opinion in Colloid & Interface Science* **2017,** *27*, 1-8.

58. Røn, T.; Lee, S., Influence of temperature on the frictional properties of water-lubricated surfaces. *Lubricants* **2014,** *2* (4), 177-192.

59. Ewen, J.; Heyes, D.; Dini, D., Advances in nonequilibrium molecular dynamics simulations of lubricants and additives. *Friction* **2018,** *6* (4), 349-386.

60. Jian, W.; Lau, D., Creep performance of CNT-based nanocomposites: a parametric study. *Carbon* **2019,** *153*, 745-756.

61. Wang, X.; Gong, L.-X.; Tang, L.-C.; Peng, K.; Pei, Y.-B.; Zhao, L.; Wu, L.-B.; Jiang, J.-X., Temperature dependence of creep and recovery behaviors of polymer composites filled with chemically reduced graphene oxide. *Composites Part A: Applied Science and Manufacturing* **2015,** *69*, 288-298.

62. Feng, D.; Li, X.; Wang, X.; Li, J.; Zhang, X., Capillary filling under nanoconfinement: The relationship between effective viscosity and water-wall interactions. *International Journal of Heat and Mass Transfer* **2018,** *118*, 900-910.

63. Lin, L.; Kedzierski, M. A., Density and viscosity of a polyol ester lubricant: Measurement and molecular dynamics simulation. *International Journal of Refrigeration* **2020,** *118*, 188-201.

64. Kestin, J.; Shankland, I. R., Viscosity of aqueous NaCl solutions in the temperature range 25–200 C and in the pressure range 0.1–30 MPa. *International Journal of Thermophysics* **1984,** *5* (3), 241-263.

Table of Contents (TOC)/Abstract Graphic:

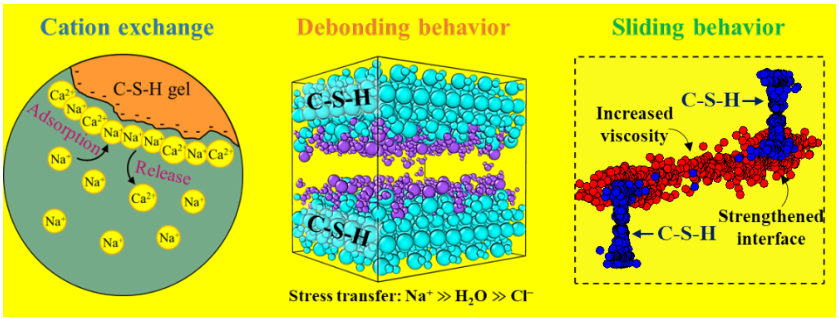

For Table of Contents Only